Numerical Simulations of Wave Generation by a Vertical Plunger Using RANS and SPH Models

S. C. Yim, M.ASCE[1]; D. Yuk[2]; A. Panizzo[3]; M. Di Risio[4]; and P. L.-F. Liu, F.ASCE[5]

Abstract: The water wave generation by a freely falling rigid body is examined in this paper. Two different two-dimensional numerical approaches have been utilized to simulate the time histories of fluid motion, free surface deformation, and the vertical displacement of a rectangular-shape rigid body. While the first approach is based on the Reynolds-averaged Navier–Stokes (RANS) equations, with the k-ϵ closure model to compute the turbulence intensity, the second uses the smoothed particle hydrodynamics (SPH) method. Numerical simulations using several different initial elevations of the rigid body and different water depths have been performed. The displacement of the moving rigid body is determined by dynamic equilibrium of the forces acting on the body. Numerical results obtained from both approaches are discussed and compared with experimental data. Images of the free surface profile and falling rigid body recorded from the laboratory tests are compared with numerical results. Good agreement is observed. Numerical solutions for the velocity fields, pressure distributions, and turbulence intensities in the vicinity of the falling rigid body are also presented. The similarity and discrepancy between the solutions obtained by the two approaches are discussed.

DOI: XXXX

CE Database subject headings: Simulation; Numerical models; Hydrodynamics; Wave generation.

Introduction

Recently, significant progress has been made in the field of numerical analysis of fluid-structure interaction problems with the aid of advanced computing technology. Numerical tools for analyzing fluid flows and structural mechanics have been developed separately using different mathematical approaches. Conventionally, the Eulerian formulation is widely used to describe fluid flows, because it is relatively easy to implement the conservation laws of flow motions. On the other hand, the Lagrangian formulation has been a predominant approach in the development of numerical tools for structural mechanics because of the convenience in using the Lagrangian description for the material surface displacement and the dynamic response of the structural system. Recently, the mixed or arbitrary Eulerian–Lagrangian formulation, which is necessary for coupling fluid and structural dynamic problems (Belytschko et al. 2000), has been used widely in developing a numerical model for fluid-structure interactions.

In studying fluid-structure interaction problems, it is essential to fully couple the motions of the structure and the ambient fluid flows. In an earlier study by Yuk et al. (2006), a numerical model has been developed, in which the coupling between the moving rigid body and fluid flows is based on an iterative procedure enforcing the principle of the dynamic equilibrium of the fluid, the structure, and their interfaces. In other words, the displacement of the structure and the fluid are determined in such a way that the dynamic equilibrium on the interface between fluid and rigid body is satisfied simultaneously at each time step. We note that the model presented by Yuk et al. (2006) is an extension of the Reynolds-averaged Navier–Stokes (RANS) model originally developed by Lin and Liu (1998a, b) for studying breaking waves in surf zone. A k-ϵ nonlinear eddy viscosity closure model was used in describing the statistical properties of turbulence. In Lin and Liu's model the volume of fluid (VOF) method is used to track the free surface locations. This model has been employed to investigate various problems concerning wave forces acting on stationary structures (e.g., Liu et al. 1999; Chang et al. 2001, 2005; Hsu et al. 2002; Liu and Al-Banaa 2004).

Smoothed particle hydrodynamics (SPH) is a numerical model based on a fully Lagrangian approach. SPH has been used in the last decade to model fluid flows considering the fluid as being made up of a finite number of particles, evolving in a mesh-free domain. Applications of SPH to modeling of landslide generated water waves have been successfully carried out by Monaghan and Kos (2000), Monaghan et al. (2003), Panizzo (2004a,b), and Panizzo and Dalrymple (2004).

In the present paper, the RANS model developed by Yuk et al. (2006) and the SPH model developed by Panizzo (2004a,b) are both applied to predict the aerial and submerged drop of a rigid

[1]Professor, Ocean Engineering Program, Civil Engineering Dept., Oregon State Univ., Corvallis, OR 97331 (corresponding author). E-mail: solomon.yim@oregonstate.edu

[2]Staff Engineer, BSM Consulting Engineers, Inc., Astoria, OR 97103; formerly, Post Doctoral Student, Ocean Engineering Program, Civil Engineering Dept., Oregon State Univ., Corvallis, OR 97331.

[3]Post Doctoral Student, DISAT Dept., L'Aquila Univ., 67040 Monteluco di Roio, L'Aquila, Italy.

[4]Post Doctoral Student, Dept. of Civil Engineering, Tor Vergata Univ., Via del Politecnico 1, 00133 Rome, Italy.

[5]Professor, School of Civil and Environmental Engineering, Cornell Univ., Ithaca, NY 97331.

Note. Discussion open until October 1, 2008. Separate discussions must be submitted for individual papers. To extend the closing date by one month, a written request must be filed with the ASCE Managing Editor. The manuscript for this paper was submitted for review and possible publication on March 7, 2006; approved on September 12, 2006. This paper is part of the ***Journal of Waterway, Port, Coastal, and Ocean Engineering***, Vol. 134, No. 3, May 1, 2008. ©ASCE, ISSN 0733-950X/2008/3-1–XXXX/$25.00.

body and the subsequent generation and propagation of waves. To demonstrate their accuracy and capability, numerical results from these models are compared with a set of experimental data. Specifically, the experiments involved dropping a weighted box vertically into a body of water. The experimental study was carried out in the framework of a research program on tsunami generation and propagation, performed at the LIAM laboratory of L'Aquila University (Panizzo 2004a). In the present work, the free surface deformation estimated from pictures taken during the experiments and wave gauge data are used to validate and compare the above mentioned numerical models.

The present paper is organized as follows: "Model Description" introduces the RANS and the SPH numerical models. Subsequently, "Experimental Setup" describes the experimental setup and program, while comparisons of model results and experimental data are discussed in "Numerical Results." Finally, summary conclusions are presented in the "Concluding Remarks."

Models Description

For completeness, both the RANS equations model and the SPH model are briefly described here. More details can be found in Lin (1998), Panizzo (2004a,b), and Yuk et al. (2006).

RANS Model

As shown in Lin and Liu (1998a) the ensemble averaged mean flow field is solved by using RANS equations that are given as

$$\frac{\partial \langle u_i \rangle}{\partial x_i} = 0 \tag{1}$$

$$\frac{\partial \langle u_i \rangle}{\partial t} + \langle u_j \rangle \frac{\partial \langle u_i \rangle}{\partial x_j} = -\frac{1}{\langle \rho \rangle}\frac{\partial \langle p \rangle}{\partial x_i} + g_i + \frac{1}{\langle \rho \rangle}\frac{\partial \langle \tau_{ij}^m \rangle}{\partial x_j} - \frac{\partial \langle u_i' u_j' \rangle}{\partial x_j} \tag{2}$$

where subscripts i and j (=1,2) denote Cartesian components for two-dimensional flows and $\langle\rangle$=ensemble average of the physical variables appearing in the Navier–Stokes (NS) equations. In Eqs. (1) and (2), u_i denotes ith component of the velocity vector; ρ=density of fluid; p=pressure; g_i=ith component of the gravitational acceleration; and τ_{ij}^m=molecular viscous stress tensor. For a Newtonian fluid, τ_{ij}^m, can be expressed by $\tau_{ij}^m = 2\mu\sigma_{ij}^m$ with μ being dynamic viscosity and $\sigma_{ij} = (\partial u_i/\partial x_j + \partial u_j/\partial x_i)/2$ strain rate tensor. In Eq. (2), the Reynolds stress tensor is defined as

$$R_{ij} = -\langle \rho \rangle \langle u_i' u_j' \rangle \tag{3}$$

In previous research work, many second-order turbulence closure models have been developed for different applications. In this paper, the k-ϵ model, where the Reynolds stress is approximated by a nonlinear algebraic stress model, is employed for turbulence closure (Lin and Liu 1998a; Shih et al. 1996).

$$\begin{aligned}\rho \langle u_i' u_j' \rangle = {} & \frac{2}{3}\rho k \delta_{ij} - C_d \frac{k^2}{\epsilon}\left(\frac{\partial \langle u_i \rangle}{\partial x_j} + \frac{\partial \langle u_j \rangle}{\partial x_i}\right) \\ & - \rho \frac{k^3}{\epsilon^2}\left[\begin{array}{l} C_1\left(\dfrac{\partial \langle u_i \rangle}{\partial x_l}\dfrac{\partial \langle u_l \rangle}{\partial x_j} + \dfrac{\partial \langle u_j \rangle}{\partial x_l}\dfrac{\partial \langle u_l \rangle}{\partial x_i} - \dfrac{2}{3}\dfrac{\partial \langle u_l \rangle}{\partial x_k}\dfrac{\partial \langle u_k \rangle}{\partial x_l}\delta_{ij}\right) \\ + C_2\left(\dfrac{\partial \langle u_i \rangle}{\partial x_k}\dfrac{\partial \langle u_j \rangle}{\partial x_k} - \dfrac{1}{3}\dfrac{\partial \langle u_l \rangle}{\partial x_k}\dfrac{\partial \langle u_l \rangle}{\partial x_k}\delta_{ij}\right) \\ + C_3\left(\dfrac{\partial \langle u_k \rangle}{\partial x_i}\dfrac{\partial \langle u_k \rangle}{\partial x_j} - \dfrac{1}{3}\dfrac{\partial \langle u_l \rangle}{\partial x_k}\dfrac{\partial \langle u_l \rangle}{\partial x_k}\delta_{ij}\right) \end{array}\right]\end{aligned} \tag{4}$$

where C_1, C_2, and C_3=empirical coefficients; δ_{ij}=Kronecker delta; $k = \frac{1}{2}\langle u_i' u_i' \rangle$=turbulence kinetic energy; and $\epsilon = \nu\langle (\partial u_i'/\partial x_k)^2 \rangle$=dissipation rate of turbulence kinetic energy with $\nu = \mu/\rho$=kinematic viscosity. Eq. (4) returns to classical linear isotropic eddy viscosity model when $C_1 = C_2 = C_3 = 0$ as shown below

$$\langle u_i' u_j' \rangle = -2\nu_t \langle \sigma_{ij} \rangle + \frac{2}{3}k\delta_{ij} \tag{5}$$

where $\nu_t = C_d(k^2/\epsilon)$=eddy viscosity; and C_d=another empirical coefficient. The turbulence closure model given in Eq. (4) can be applied to general anisotropic turbulent flows. The governing equation for k and ϵ (Rodi 1980) are modeled as

$$\frac{\partial k}{\partial t} + \langle u_j \rangle \frac{\partial k}{\partial x_j} = \frac{\partial}{\partial x_j}\left[\left(\frac{\nu_t}{\sigma_k} + \nu\right)\frac{\partial k}{\partial x_j}\right] - \langle u_i' u_j' \rangle \frac{\partial \langle u_i \rangle}{\partial x_j} - \epsilon \tag{6}$$

$$\frac{\partial \epsilon}{\partial t} + \langle u_j \rangle \frac{\partial \epsilon}{\partial x_j} = \frac{\partial}{\partial x_j}\left[\left(\frac{\nu_t}{\sigma_\epsilon} + \nu\right)\frac{\partial \epsilon}{\partial x_j}\right] + C_{1\epsilon}\frac{\epsilon}{k}\nu_t\left(\frac{\partial \langle u_i \rangle}{\partial x_j} + \frac{\partial \langle u_j \rangle}{\partial x}\right)\frac{\partial \langle u_i \rangle}{\partial x_j} \tag{7}$$

$$- C_{2\epsilon}\frac{\epsilon^2}{k}$$

where σ_k, σ_τ, $C_{1\epsilon}$, and $C_{2\epsilon}$=empirical coefficients. The coefficients in Eqs. (4)–(7) have been determined by performing many simple experiments and enforcing the physical realizability condition; the values for these coefficients employed by Lin and Liu (1998a): $C_1 = 0.0054$, $C_2 = -0.0171$, $C_3 = 0.0027$, $C_1 = 1.44$, $C_{2\epsilon} = 1.9$, $\sigma_\epsilon = 1.3$, and $\sigma_k = 1.0$, are also used in this study.

Applying appropriate boundary conditions, and approximating the derivatives in the Navier–Stokes equations using a finite-difference scheme with a combination of backward and forward difference methods, numerical solutions are obtained. Detailed descriptions of the numerical algorithms, such as the two-step projection method for solving RANS equations (Chorin 1968) and the VOF method for tracking free surface locations (Hirt and Nichols 1981) as well as boundary conditions can be found in a previous study by Lin and Liu (1998a).

SPH Model

SPH is a particle Lagrangian numerical model, which was first introduced in astrophysics by Lucy (1977) and Gingold and Monaghan (1977), and then adapted by Monaghan (1994) to simulate free surface fluid flows. The model is based on two fundamental ideas that every flow characteristic is smoothed over the spatial domain by using an appropriate kernel function W, and that the smoothed flow is approximated by particles, whose time evolution is governed by a Lagrangian scheme. There are no constraints imposed on the geometry of the system or on how far it may evolve from the initial conditions. The equations of fluid dynamics are transformed into integral equations by using the kernel function W, which presents a finite interaction radius equal to $2h$. The kernel is indeed a weighting function that smoothes out field contributions defining the value of a physical variable, say A, at a certain point $\mathbf{r}$. In this approach, the kernel estimate of A is defined as (Morris 1996)

$$A(\mathbf{r}) = \int_{\text{space}} A(\mathbf{r}')W(\mathbf{r} - \mathbf{r}', h)d\mathbf{r}' \tag{8}$$

The kernel function W has to satisfy the following two constraints

$$\int_{\text{space}} W(\mathbf{r}-\mathbf{r}',h)d\mathbf{r}' = 1 \quad \text{and} \quad \lim_{h\to 0} W(\mathbf{r}-\mathbf{r}',h) = \delta(\mathbf{r}-\mathbf{r}') \tag{9}$$

In other words, W=smoothing function with a compact support, approximating a Dirac delta function. In the same manner, it is possible to estimate the gradient of a given function as (Morris 1996; Schlatter 1999)

$$\nabla_{\mathbf{r}} A(\mathbf{r}) = \int_{\text{space}} A(\mathbf{r}')\nabla_{\mathbf{r}} W(\mathbf{r}-\mathbf{r}',h)d\mathbf{r}' \tag{10}$$

In the SPH numerical implementation, the fluid domain is represented by a certain finite number of particles, carrying the physical variable at the points occupied by their volumes. Starting from Eqs. (8) and (10), if we refer to a finite number of particles in a finite domain, under the hypothesis that the kernel, the variable, or both go to zero at infinity, it is possible to write the SPH estimation of the physical variable A and its gradient as a summation over neighbors b of particle a, such as

$$A_a = \sum_{b=1}^{N} V_b A_b W_{ab}, \quad \text{and} \quad \nabla_a A_a = \sum_{b=1}^{N} V_b A_b \nabla_a W_{ab} \tag{11}$$

where $W_{ab}=W(\boldsymbol{r}_a-\boldsymbol{r}_b,h)$; $V_i=m_i/\rho_i$; and ∇_i implies spatial derivative with respect to coordinates of the generic particle i.

It can be demonstrated (Morris 1996; Schlatter 1999) that the gradient of the physical variable A at hand can be rewritten as

$$\nabla_a A_a = \frac{1}{\rho_a}\sum_{b=1}^{N} m_b(A_b - A_a)\nabla_a W_{ab} \tag{12}$$

Using this approximation process, it is possible to rewrite the continuity equation as

$$\frac{d\rho_a}{dt} = \sum_{b=1}^{N} m_b(\mathbf{v}_a - \mathbf{v}_b)\nabla_a W_{ab} \tag{13}$$

The momentum equation for an inviscid and compressible fluid (Euler equation) reads

$$\frac{d\mathbf{v}_a}{dt} = -\sum_{b=1}^{N} m_b\left(\frac{P_b}{\rho_b^2} - \frac{P_a}{\rho_a^2}\right)\nabla_a W_{ab} \tag{14}$$

In the present work we take into account a real fluid $\nabla_{\mathbf{r}'}$ by rewriting Eq. (14) as suggested by Monaghan (1994), as

$$\frac{d\mathbf{v}_a}{dt} = -\sum_{b=1}^{N} m_b\left(\frac{P_b}{\rho_b^2} - \frac{P_a}{\rho_a^2} + \prod_{ab}\right)\nabla_a W_{ab} \tag{15}$$

where Π_{ab}=artificial viscous pressure and it is defined as

$$\prod_{ab} = \begin{cases} \dfrac{-\alpha c_{ab}\mu_{ab} + \beta\mu_{ab}^2}{\rho_{ab}} & \text{if } \mathbf{v}_{ab}\cdot\mathbf{r}_{ab} < 0 \\ 0 & \text{otherwise} \end{cases} \tag{16}$$

with $\mu_{ab}=h\mathbf{v}_{ab}\cdot\mathbf{r}_{ab}(\mathbf{r}_{ab}^2+\eta^2)$; $\rho_{ab}=(\rho_a+\rho_b)/2$; $c_{ab}=(c_a+c_b)/2$; c_a and c_b=speed of sound evaluated at particles a and b positions; h=smoothing length; $\eta^2=0.01h$; and α and β=constants usually assuming values $\alpha=0.01$; $\beta=0.0$ for general hydraulic problems.

In this paper the kernel function proposed by Johnson et al. 1996) is employed, because it is well suited to simulate impacts between rigid bodies and the water. It is defined in the range $s=r/h\in[0.0;2.0]$, as

$$W(\mathbf{r},h) = \frac{1}{\pi h^2}\left(\frac{3}{8}s^2 - \frac{3}{2}s + \frac{3}{2}\right)$$

$$W'(\mathbf{r},h) = \frac{1}{\pi h^3}\left(\frac{3}{4}s - \frac{3}{2}\right) \tag{17}$$

A state equation, defined as $p=B[(\rho/\rho_o)^{\gamma}-1]$, with $\gamma=7.0$ and $\rho_o=1,000.0$ kg/m^3, is used in the model to relate density and pressure.

Experimental Setup

A series of experiments for water wave generation by a solid body plunger (Scott Russell wave generator) has been conducted at LIAM laboratory, L'Aquila University, Italy (Di Risio 2005). The experiments were performed in a three-dimensional flume 12 m long, 0.45 m deep, and 0.3 m wide (see Fig. 1). Rectangular cylinders with width=0.3 m (same as flume), height=0.1 m (vertical direction), and variable length (in flume direction, see Table 1 and Fig. 1) are released vertically at one end of the flume to generate waves. The space between the cylinder and the vertical walls of the flume is less than 1 mm. The specific weight of the cylinder is 1.33 t/m^3. Three lengths of rectangular rigid body (0.05, 0.1, and 0.15 m) are used. Twenty one tests were conducted (see Table 1). Three different initial elevations of the cylinder are tested: partially submerged (the bottom of the cylinder is 3 cm below the still water level); on the still water level; and aerial (3 cm above the still water level). The water depth in the flume is also varied: 6, 10, 18, and 23 cm. Among these tests, three representative cases (L10H10M3, L10H10P3, and L10H18P3) are discussed in this paper.

During the experiments, five wave gauges are installed along the flume to measure the free surface elevation. A digital video camera (Canon XM1) with a frame acquisition rate of 25 Hz is used to record the wave profile in the generation region.

Numerical Results

The free falling rectangular body and the subsequent wave generation and propagation are modeled in the two-dimensional (2D) vertical plane. For the RANS model, a computational domain of 1.4 m$\times$0.4 m is discretized with uniform grid size of 0.5 cm in horizontal direction and 0.25 cm in vertical direction. A rectangular shape rigid body is placed at the left end of the domain at a given height relative to the still water free-surface level and allows falling under gravity. Free-slip boundary conditions are applied on all the boundaries except at the right end of the computational domain, where the radiation boundary condition is imposed so as to ensure outgoing waves through the boundary. The same k-ϵ model is used for the boundary layer on the solid boundary including a vertical plunger.

In the numerical simulations, it is assumed that there is no space between the rigid boundary of the falling cylinder and the left boundary of the computational domain and the motion of falling body is always in perfectly vertical direction without rotation. The frictional forces acting on the surfaces of the box that are in contact with the vertical wall of the flume are assumed to be proportional to the contact area of the body with the wall, i.e., larger frictional forces are used for the box with larger dimension. The dynamic coefficient of friction used for the computation of three representative cases is $\mu=0.66$.

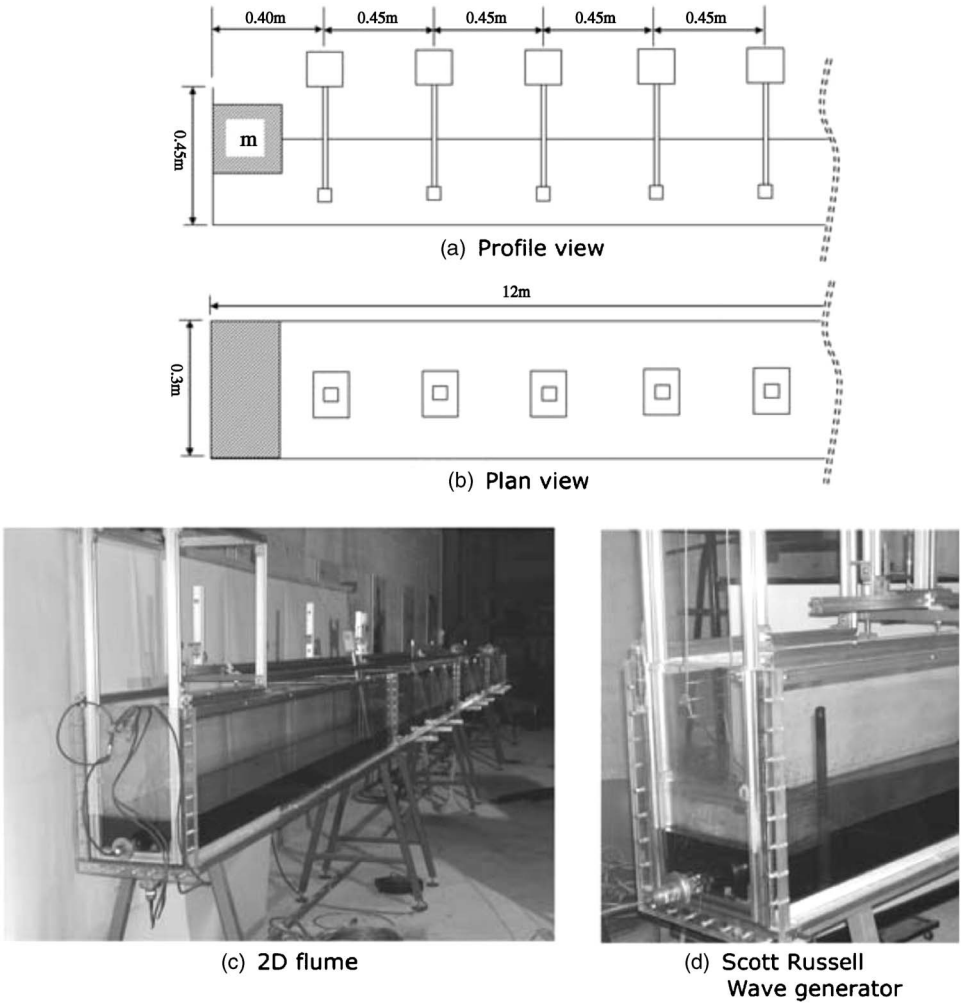

Fig. 1. (a), (b) Locations of wave gauges; (c) picture of 2D flume; and (d) Scott Russell wave generator

In computing the total force on the falling cylinder, the shear stress induced by flow motions, which is applied in a tangential direction on the moving boundary, is assumed to be negligible. Thus, only the normal forces obtained by integrating pressures along the moving boundaries are considered in this study. Motion of the cylinder for the RANS model is advanced by solving dynamic equilibrium. The validity of the shear force assumption will be examined in a later section and further discussed in the "Concluding Remarks."

For the SPH model, numerical simulations have been carried out using a computational domain of 2.0 m × 0.5 m, with particle diameter equal to 0.004 m. Initially, particles have been placed on a regular grid, with uniform grid size of 0.004 m. Boundaries and the rigid box falling into water have been modeled using repellent particles (Monaghan 1994), with free-slip conditions on all surfaces. In all simulations, the α parameter assumed the value $\alpha = 0.07$. Motion of the cylinder for the SPH model is prescribed by the experimental data. No dynamic equilibrium is considered.

For both RANS and SPH models, mesh regeneration is not required during the simulation. The same rectangular mesh in Cartesian coordinate is used with moving boundary condition throughout the simulation.

Three-dimensional effects are observed in some of the experiments. Differences in the free-surface elevation on one side wall of tank and the other side wall were noticed. However, these 3D effects occurred when the wave was propagating after the wave generation. It is noted that 3D effects are negligible in the wave generation region.

For the numerical simulations and comparisons presented in the following sections, the Reynolds numbers ranges from 2.3e+4 to 5.9e+4, the Froude number from 0.22 to 0.42, and simulation step sizes range from 0.0005 to 0.005, respectively.

Comparisons of RANS and SPH Model Predictions

Three selected cases of the physical experiments are presented in this section to examine the prediction capabilities between the two numerical models. The same rigid body is employed in all three cases. However, Cases I and II have identical water depths but different initial rigid body vertical locations. In Case I, the bottom of the rigid body is initially below the still water lever (SWL) whereas in Case II, the bottom of the body is above the SWL. For Case III, the bottom of the rigid body has identical initial height with respect to the SWL as in Case II. However, the body is dropped into a large water depth.

Case I

In the first representative case (referred to as Test L10H10M3), the rigid body with dimensions of 0.1 m × 0.3 m × 0.1 m (length × width × height) is located initially 3 cm below the SWL

Table 1. Experiments Configurations

Initial box location (cm)	Box length (cm)	Water depth (cm)	Test
+3	5	6	L5H6P3
		10	L5H10P3
	10	6	L10H6P3
		10	L10H10P3
		18	L10H18P3
		23	L10H23P3
	15	6	L15H6P3
−3	5	6	L5H6M3
	10	6	L10H6M3
		10	L10H10M3
		18	L10H18M3
		23	L10H23M3
	15	6	L15H6M3
0	5	6	L5H6PM0
		10	L5H10PM0
		18	L5H18PM0
	10	6	L10H6PM0
		10	L10H10PM0
		18	L10H18PM0
		23	L10H23PM0
	15	6	L15H6PM0

and is released into the 0.1 m deep water. The time history of box displacement computed based on the RANS model is compared with experimental data in Fig. 2. Very good agreement is observed. We remark here that the numerically simulated displacement of the falling rigid body does not reach the bottom of the flume. In both SPH and RANS, simulation of the rigid body motion based on dynamic equilibrium is stopped when the bottom of the rigid body reaches a distance less than the particle diameter, in the case of SPH, and the last computational cell height, in the case of RANS, above the bottom of the flume to avoid numerical instability. After this time step, consistent with the physics of the experiment, the rigid body is held in place while simulation of the fluid dynamic continues. This procedure is applied to simulations for all cases examined in this paper. The numerical instability and the limitation of the model will be further discussed later in this paper.

A snapshot of the free surface profile and the location of the cylinder at $t=0.32$ s is also shown in Fig. 2. The numerical (RANS) solutions for the locations of boundaries of the rigid body and the free surfaces are shown in thick solid lines, which are overlapped on the experimental image for direct comparisons. Again, very good agreement with experimental data is observed.

The time series of the free surface elevation at $x=0.4$ and 0.85 m of Test L10H10M3 for both RANS and SPH numerical predictions are shown together with the measured experimental data in Fig. 3. The generated wave is a solitary-like wave with small trailing waves. Both numerical predictions match the experimental results well, with the SPH model being slightly more dissipative, resulting in a less oscillatory motion of the free surface after the main wave has passed. The calculated maximum wave heights at both stations show good agreement with experimental data. However, a slight phase difference is observed, which could be caused by the different reference times used in the experiment measurements.

Figs. 4 and 5 show the predicted pressure and velocity fields, respectively, of the RANS and SPH models at various times. While the rigid body is falling, high pressures are observed at the bottom left corner of the flume, where the velocity is diminishing, and at the same time flow separation occurs at the bottom right corner of the moving body as shown in the snapshots at $t=0.2$ s of Figs. 4 and 5. Subsequently, a large counterclockwise vortex is generated in the front of the moving body (see Fig. 5). The RANS model results show that the vortex is advected downstream (positive x direction) with a much slower speed than the phase speed of the generated solitary-like wave. Furthermore, the SPH results indicate that the vortex is attached to the front face of the rigid body until the body reaches the bottom of the flume. This discrepancy in two numerical results needs to be further examined with velocity measurements. We also observe that the pressure near the vortex center is less than the hydrostatic pressure.

Case II

In the second case (Test L10H10P3), the rigid body size and water depth are the same as those in Case I. However, the initial elevation of the bottom of the cylinder is 3 cm above the SWL.

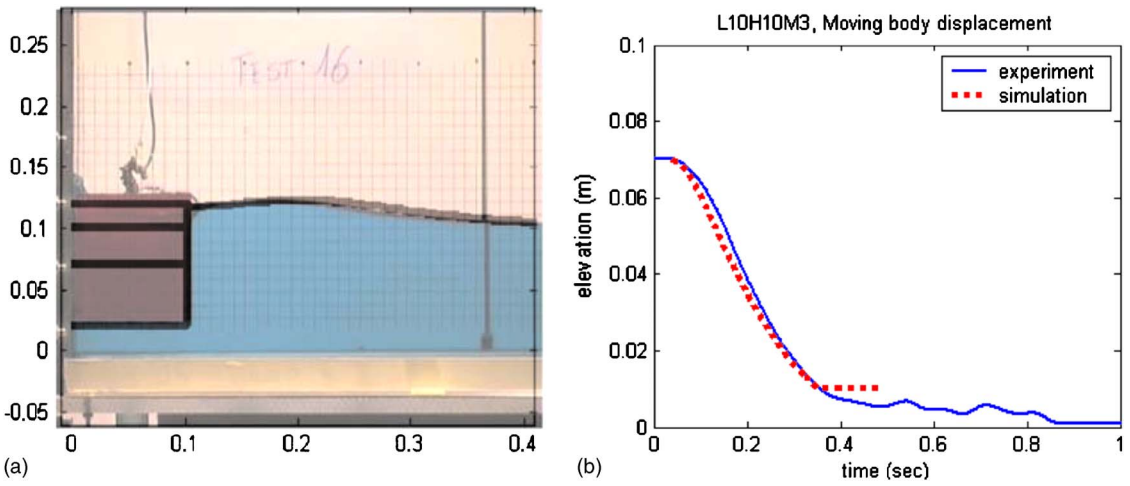

Fig. 2. Snapshot of rigid body with free surface profile at $t=0.32$ s (a); time history of rigid body displacement (b) (Case I, Test L10H10M3)

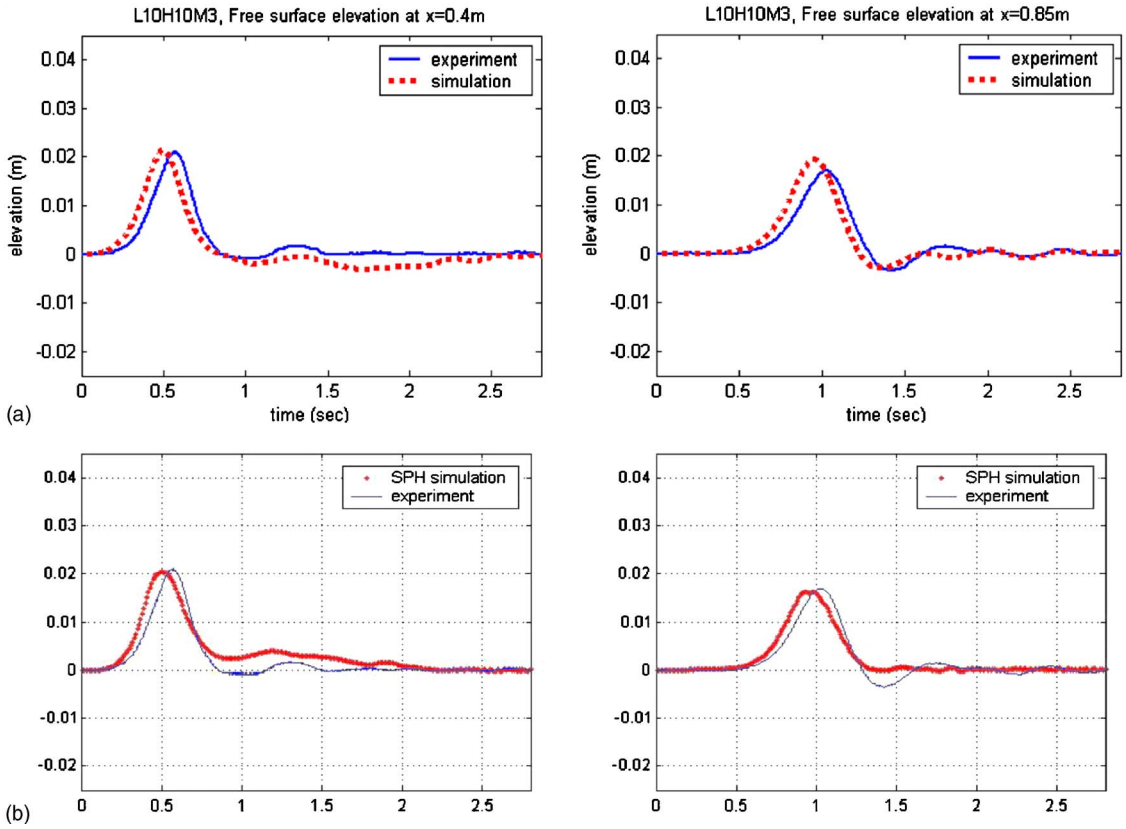

Fig. 3. Time histories of free surface elevation at $x=0.4$ and 0.85 m obtained from RANS model (a); SPH model (b) (Case I, Test L10H10M3)

The numerical results and experimental data for the movement of the falling cylinder and the snapshot of the free surface profile at $t=0.32$ s are shown in Fig. 6. Since the initial elevation of the cylinder is above the SWL, as the cylinder impacts and enters the water body, violent flow motions and free surface splashing occur. As shown in Fig. 6, the RANS model predicts the free surface reasonably well except that the splash height is underpredicted, which could be caused by the lack of required grid resolution in the numerical model. The time histories of free surface displacement at $x=0.4$ and 0.85 m are plotted in Fig. 7. It is clear that because the initial potential energy of this case is larger than that of the previous case, larger waves (the wave height to water depth ratio is about 0.4 at $x=0.4$ m) are generated near the plunging cylinder and the leading wave attenuates significantly between these two wave gauge locations (the wave height to water depth ratio is reduced to 0.3 at $x=0.85$ m). Furthermore, the amplitude dispersion seems to play an important role since the width of the leading wave has increased. The numerical results obtained from both the RANS and SPH models show slightly faster propagation speeds. As shown in Figs. 8 and 9, the influence of the falling rigid body on the fluid motion is much stronger than in the previous case with an initially submerged location. The free surface in the front face of the moving body is separated during the impact and higher pressures near the bottom left corner of the flume are observed as in the previous case.

Case III

In the third case (Test L10H18P3), the same size of cylinder is initially located 3 cm above the SWL and released into 0.18 m deep water, which is deeper than that in the previous two cases. The snapshot in Fig. 10 shows the position of falling rigid body and the free surface profile generated at $t=0.32$ s. The numerical results are in reasonably good agreement with the experimental data. Up to the point when the top of the falling rigid body is at the SWL, the pressure and velocity fields show behavior similar to those in Case II (Figs. 12 and 13). However, since the water depth is larger than the height of the falling cylinder, as the cylinder moves farther downwards (i.e., the top of cylinder becomes below the SWL) it is overtopped by a wave propagating towards the left end of the flume, which is then reflected back into the flume. Splashing at the end wall with strong turbulence intensity is observed (see Figs. 12 and 13). Unlike in the previous two cases, the vortex generated in front of the falling cylinder remains attached throughout the entire process. Discrepancy between numerical results and the experiment data are noticeable in comparisons of the time histories of free surface elevation after $t\approx 1.5$ s (see Fig. 11). While the amplitude and phase of the leading wave is predicted accurately by both models, the RANS model results show a significant phase lag at the location $x=0.4$ m. On the other hand, the SPH model does not predict well the amplitude of the third and higher trailing waves at the location $x=0.4$ m and the shape of the second and higher trailing waves at the location $x=0.85$ m. We remark here that the random nature of the splashing fluid particles and 3D air bubbles observed in the experiments might cause these discrepancies.

Turbulence Intensity

A study of the turbulence behaviors induced by different falling heights and bodies (i.e., Cases I–III) is presented in this section. Only results from RANS model predictions are examined here because turbulence intensity predictions from direction SPH computation and measured turbulence data are not available.

Fig. 14(a) shows the time evolution of the turbulence intensity

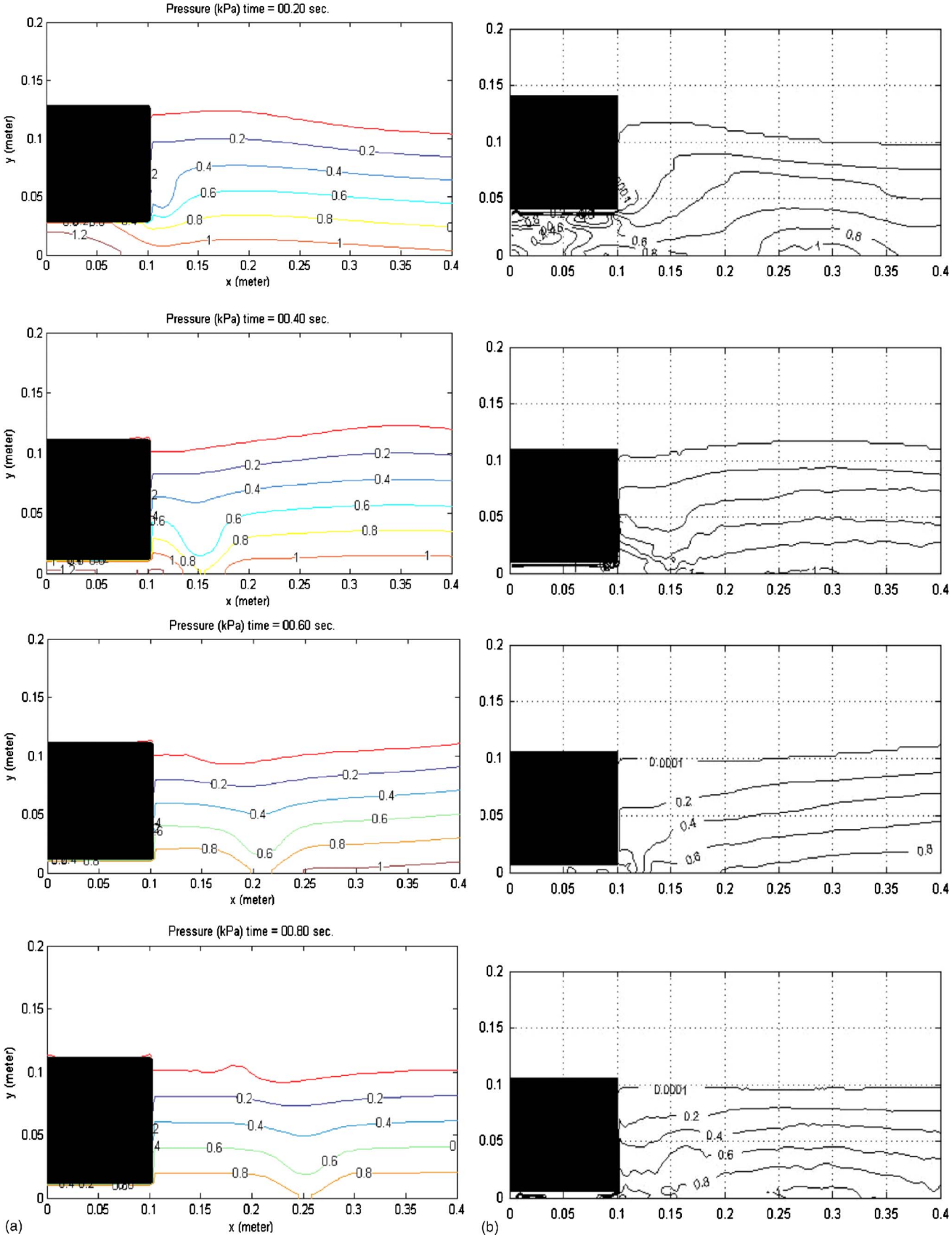

Fig. 4. Contour plots of pressure field computed by RANS (a); SPH (b) models at t=0.2, 0.4, 0.6, and 0.8 s (Case I, Test L10H10M3)

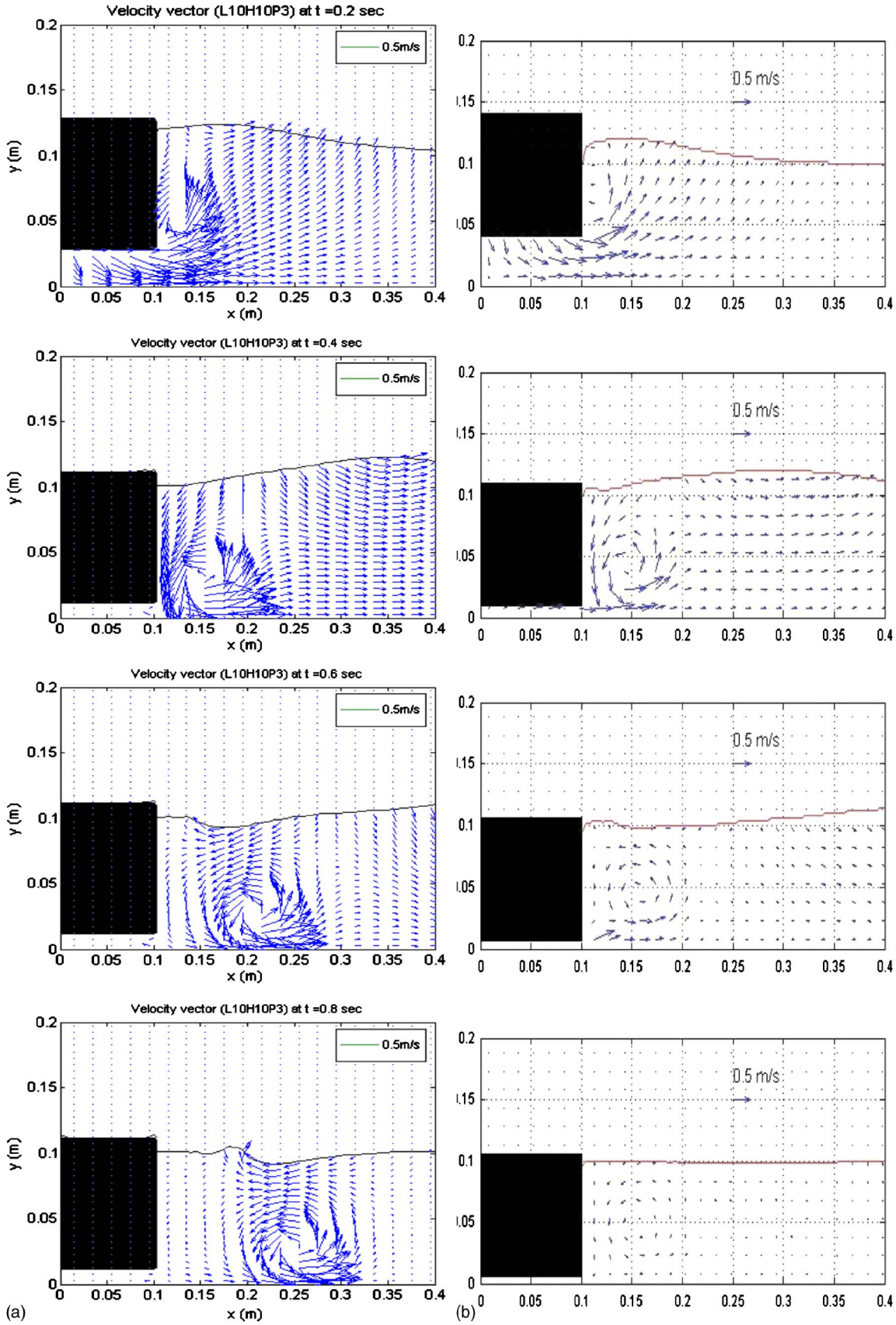

Fig. 5. Vector plots of velocity field computed by RANS model (a); SPH model (b) at t=0.2, 0.4, 0.6, and 0.8 s (Case I, Test L10H10M3)

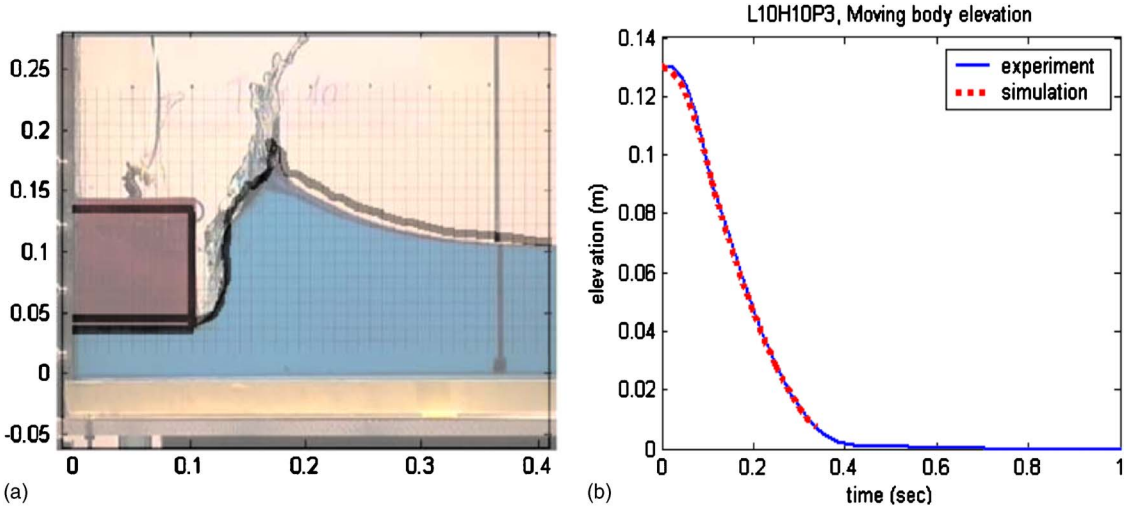

Fig. 6. Snapshot of position of rigid body and free surface profile at $t=0.32$ s (a); displacement time history of moving rigid body (b) (Case II, Test L10H10P3)

for Case I. Note that, for the initially submerged bottom drop, turbulence is generated at the bottom surface as the fluid below the falling rigid body is being pushed aside and a vortex is formed (where the turbulence intensity is the highest) at the sharp corner as expected. Based on an examination of the numerical data (not shown here due to space limitation) the turbulence intensity increases as the rigid block continues to fall, and as shown in the figure, the vortex becomes detached from the rigid body once its motion stopped. The vortex then attaches to the bottom boundary and propagates downstream with the surface wave created. The turbulence intensity decreases as the vortex moves further downstream due to energy dissipation.

In Case II, because of the higher initial elevation and in air acceleration of the body, the maximum pressure and turbulence intensity obtained were higher than the initially submerged rigid body drop test of Case I as anticipated. In fact, as shown in Fig. 14(b), in addition to the turbulence intensity generated at the rigid body bottom surface, higher turbulence intensity also occurs at

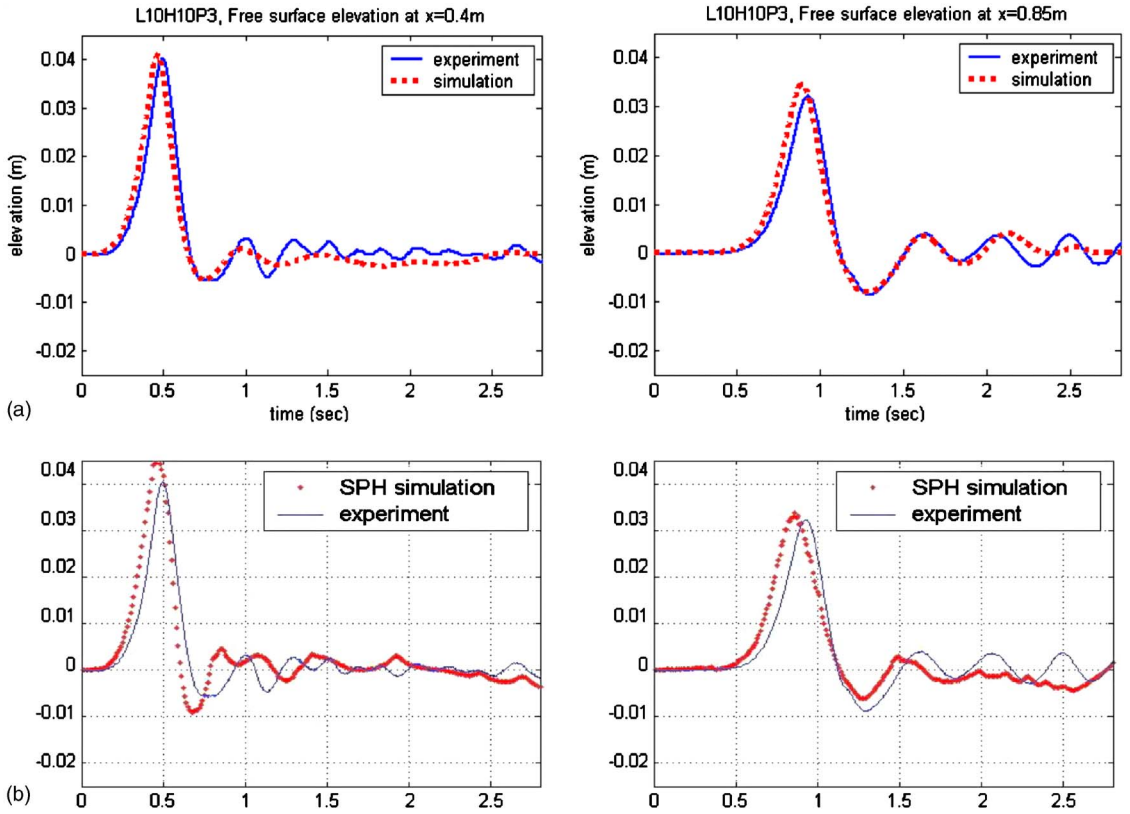

Fig. 7. Experimental data and numerical results [RANS model in (a); SPH model in (b)] for time histories of free surface elevation at $x=0.4$ and 0.85 m (Case II, Test L10H10P3)

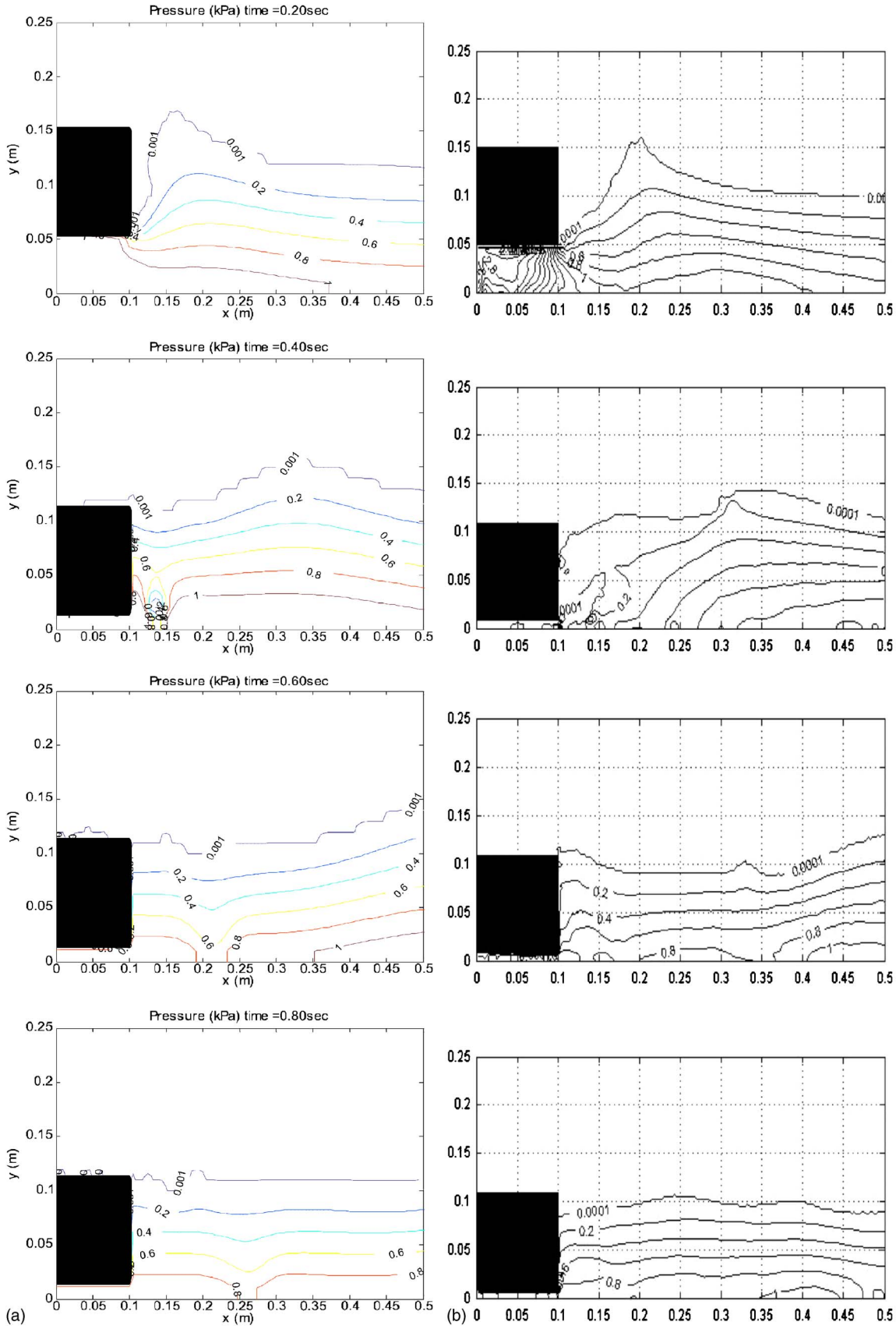

Fig. 8. Contour plot of pressure field computed by RANS (a); SPH (b) at t=0.2, 0.4, 0.6, and 0.8 s (Case II, Test L10H10P3)

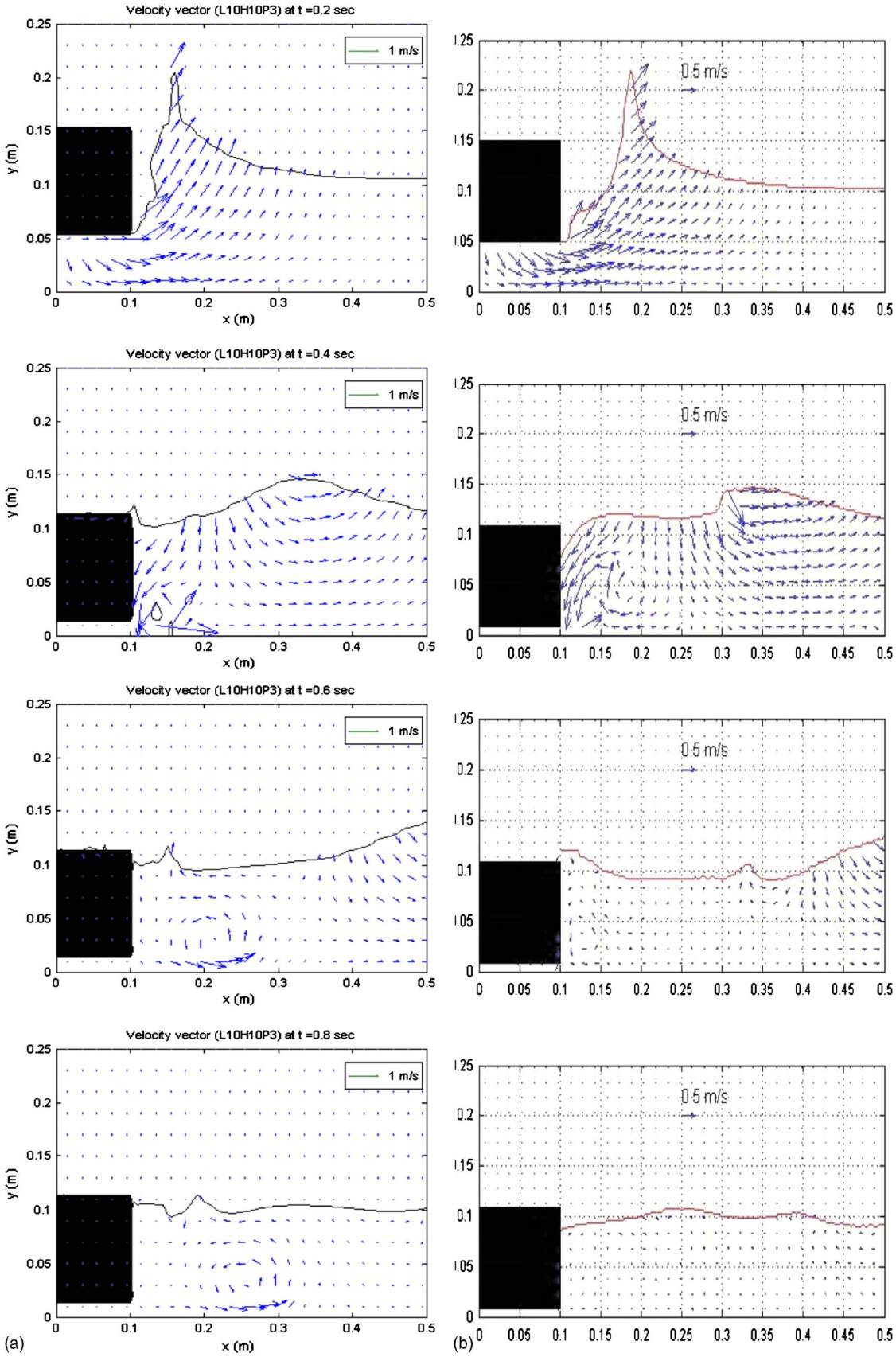

Fig. 9. Vector plot of velocity field computed by RANS (a) model; SPH (b), model at $t=0.2$, 0.4, 0.6, and 0.8 s (Case II, Test L10H10P3)

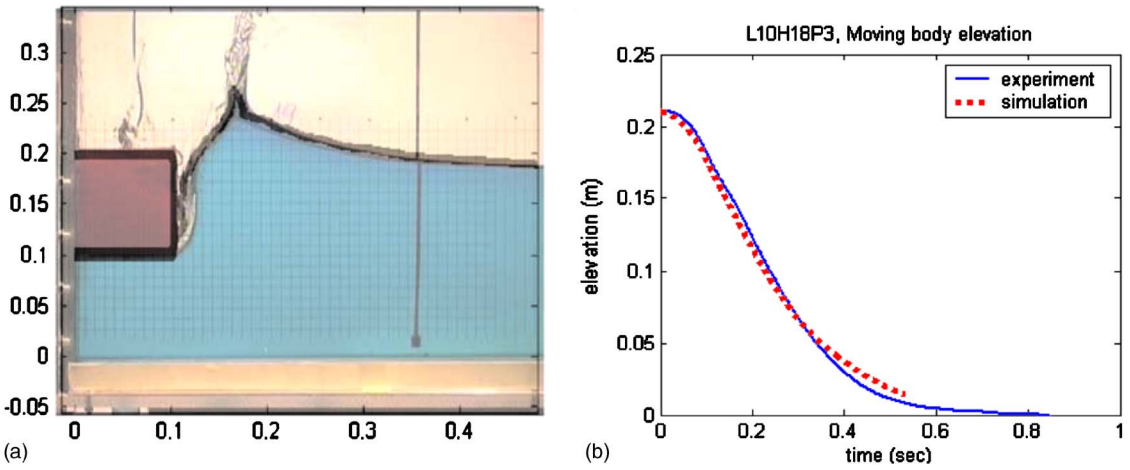

Fig. 10. Snapshot of position of rigid body and free surface profile at $t=0.32$ s (a); displacement time history of moving rigid body (b) (Case III, Test L10H18P3)

the free surface of the wave, which is separated from the vertical body surface on the right hand side. After the falling motion of the rigid body has ceased, the vortex generated at the sharp corner propagates downstream as in Case I discussed above. By the time $t=0.8$ s, the vortex has not traveled as far downstream as that in Case I and turbulence at the rigid body surface still persists.

Fig. 14(c) shows the time evolution of the turbulence intensity of the fluid in the vicinity of the falling rigid body for Case III. As expected, the initial fluid flow and turbulence behavior for this case are identical to that of Case II because of identical body and initial elevation with respect to the SWL [see top diagrams of Figs. 14(b and c), $t=0.2$ s], and fluid motion has not yet propagated to the bottom of the shallower depth, thus the difference in bottom boundary conditions (different depths) has no influence on the flow. The flow and turbulence behaviors of Case III begins to differ from those of Case II when the influence of the bottom boundary of Case II becomes noticeable, as shown in $t=0.4$ s in Figs. 14(b and c). At this time, the motion of the rigid body in Case II has stopped and the vortex at the sharp corner begins to propagate downstream. However, for Case III, the rigid body is still falling and the fluid originally displaced by the falling body returned over the top of the body with high turbulence intensity. As the rigid body continues to fall to a large depth, the vortex

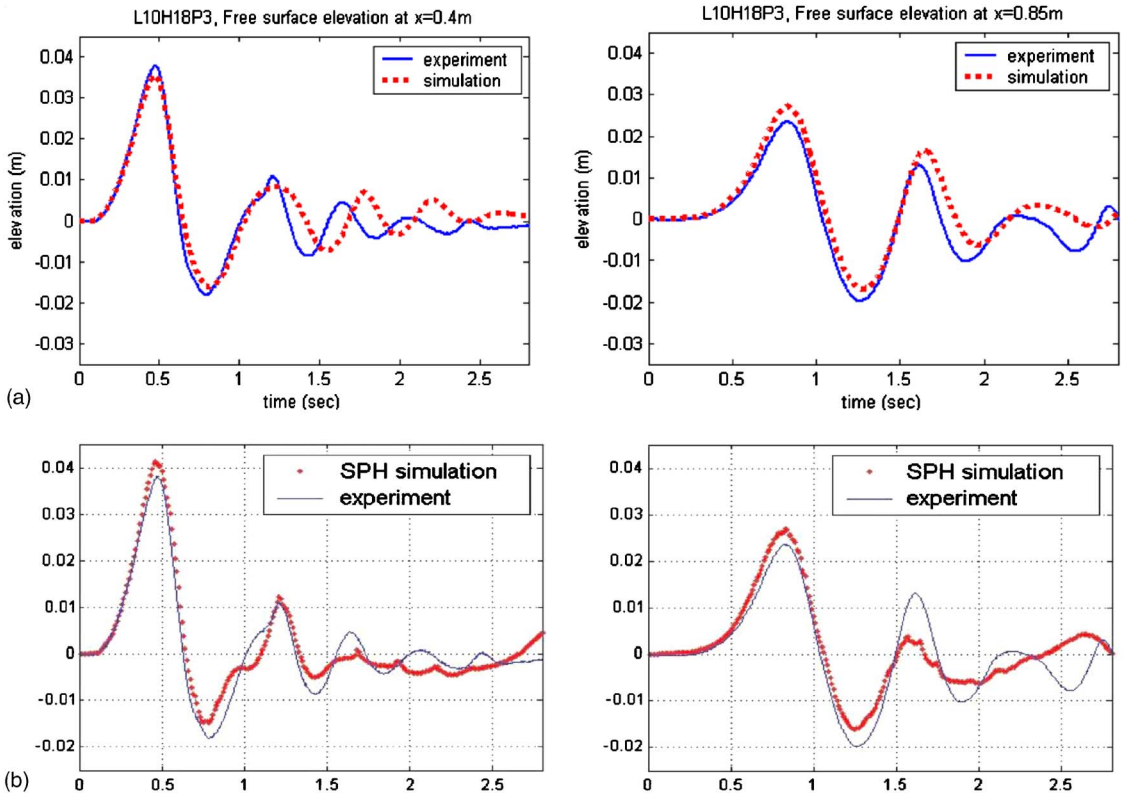

Fig. 11. Contour plot of pressure field computed by RANS model (a); SPH model (b) at $t=0.2$, 0.4, 0.6, and 0.8 s (Case III, Test L10H18P3)

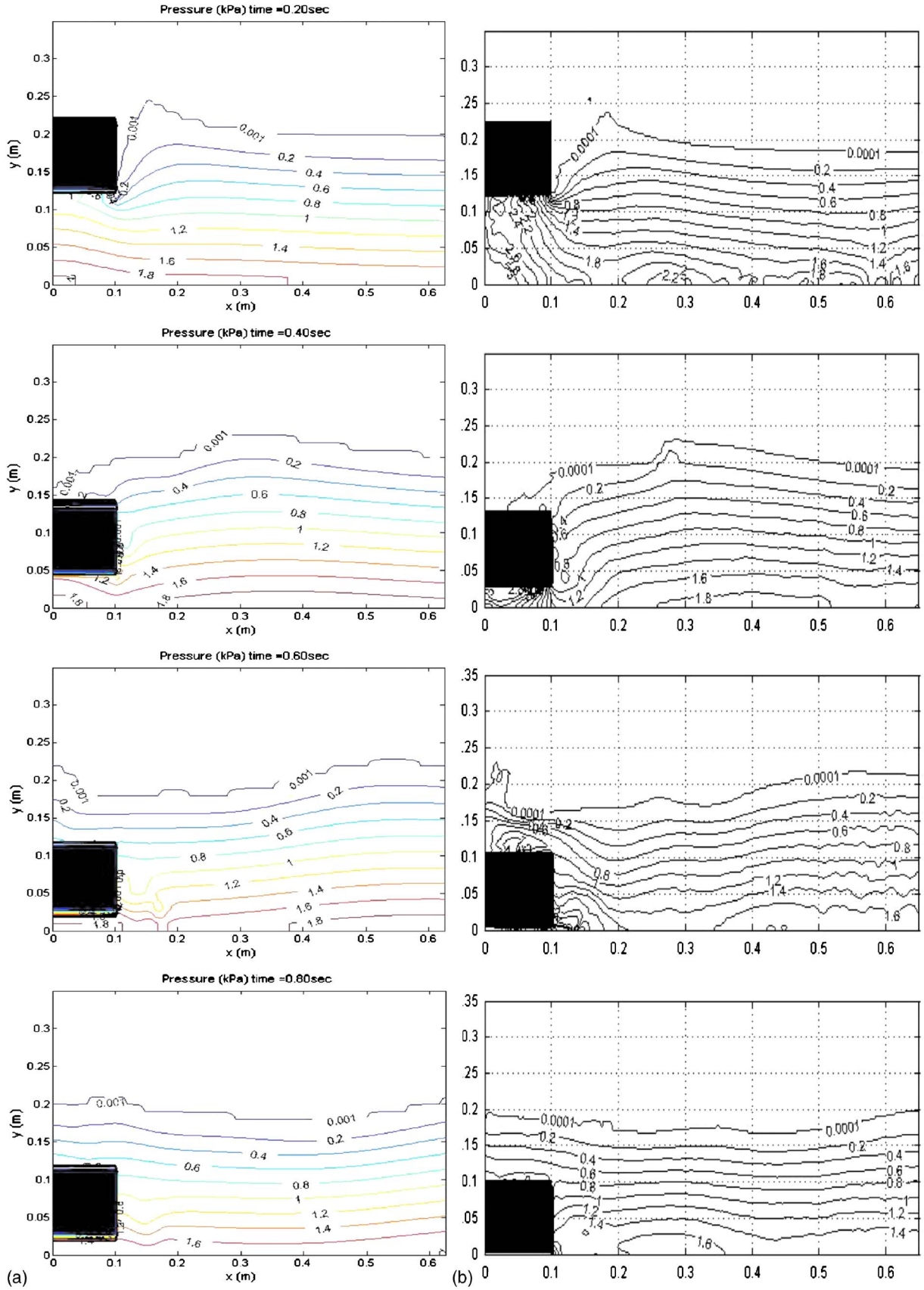

Fig. 12. Vector plot of velocity field computed by RANS model (a); SPH model (b) at $t=0.2$, 0.4, 0.6, and 0.8 s (Case III, Test L10H18P3)

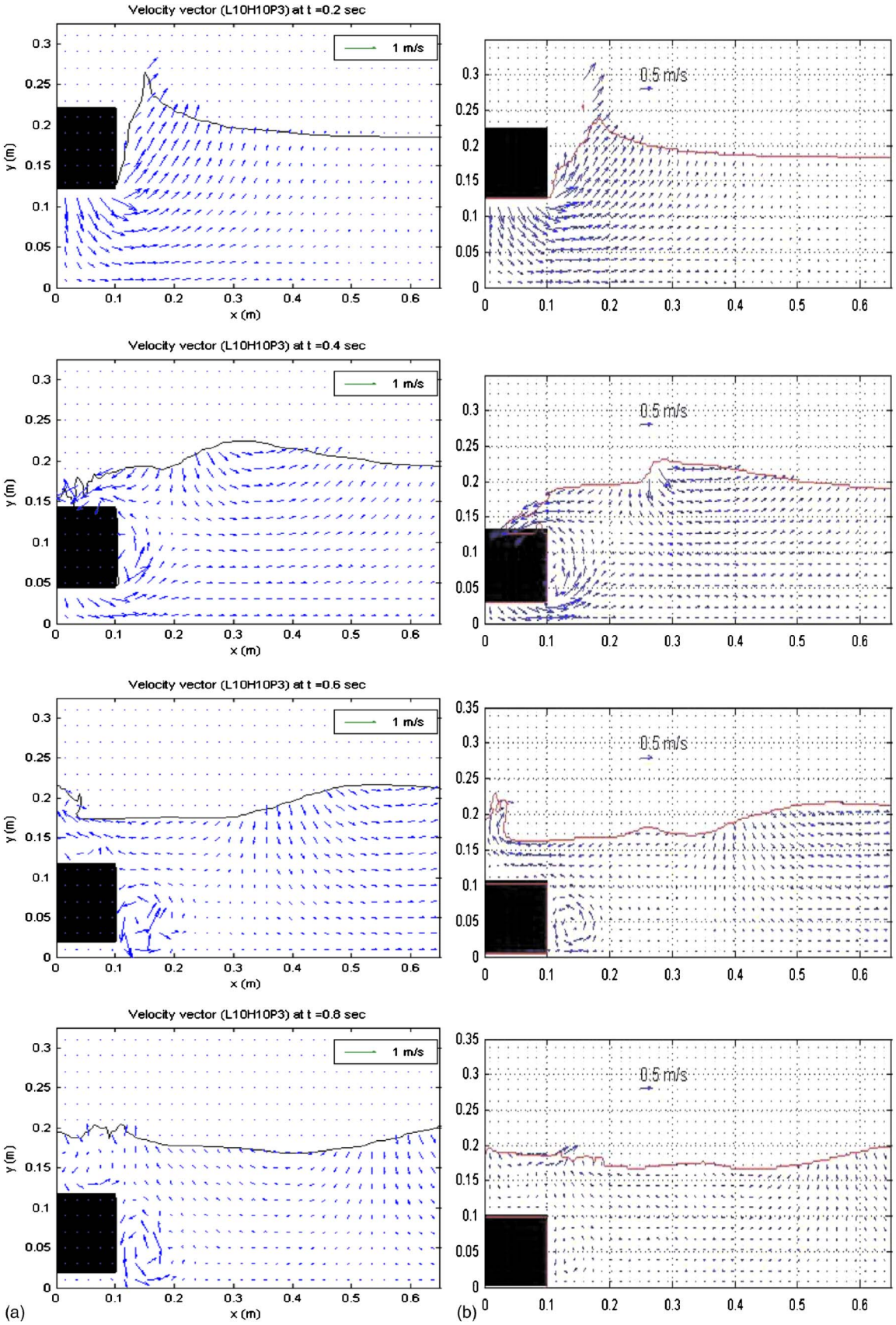

Fig. 13. Experimental data and numerical results [RANS model in (a); SPH model in (b)] for time histories of free surface elevation at $x=0.4$ and 0.85 m (Case III, Test L10H18P3)

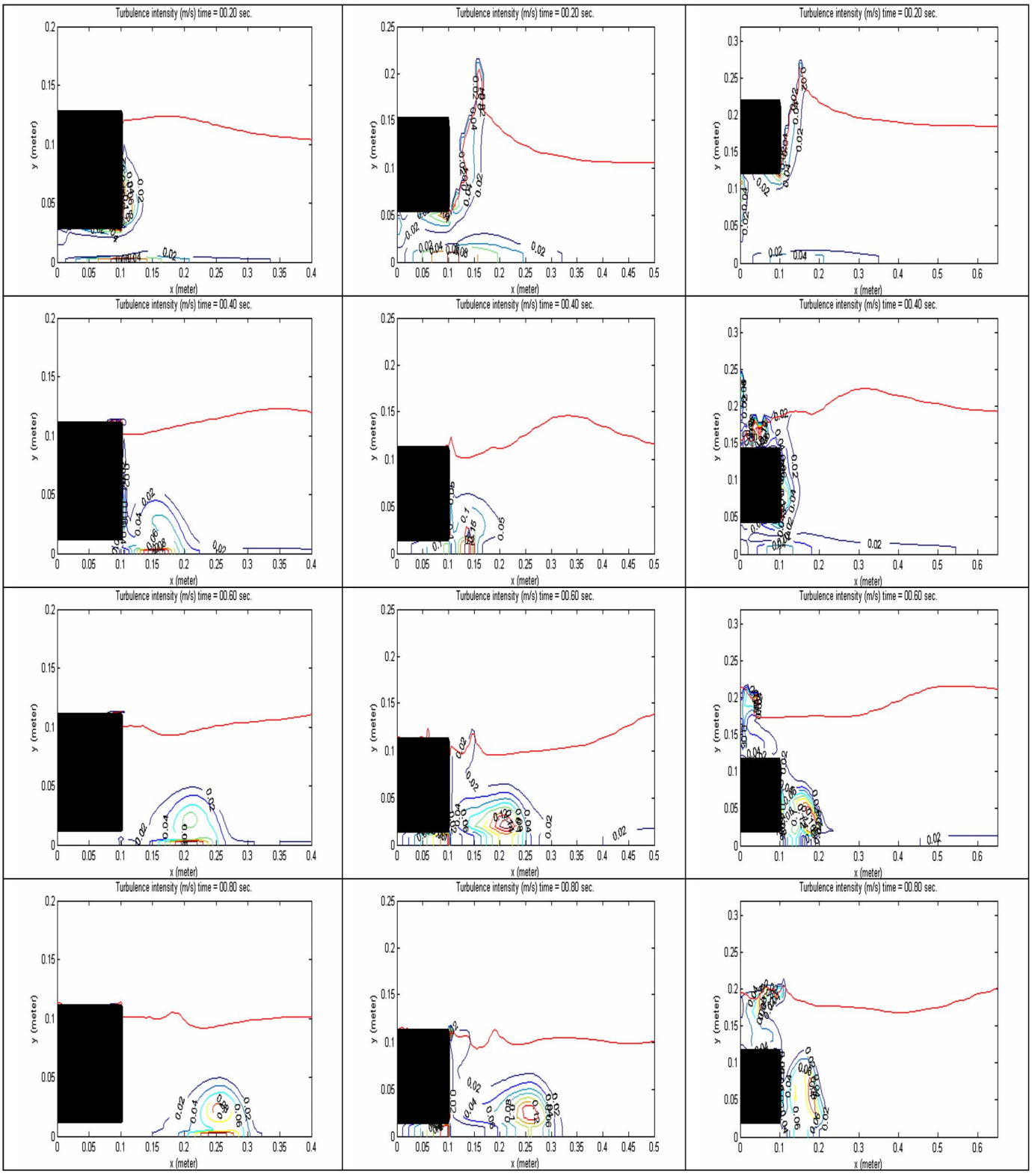

Fig. 14. Turbulence intensity (m/s) computed by the RANS model at $t=0.2$, 0.4, 0.6, and 0.8 seconds: (a) Case I, Test L10H10M3; (b) Case II, Test L10H10P3; and Case III, Test L10H18P3 (note the vertical and horizontal scales are different for the three cases

generated at the sharp edge continues to intensify and thus has the highest strength among the three cases [see Fig. 14(c) for $t=06$ and 0.8 s].

Note that energy dissipation can be observed in all three cases when the body motion has ceased and the vortex leaves the edge and begins to propagate downstream. We want to point out that a validation of the turbulence intensity model capability cannot be provided in this study because of the lack of experimental velocity field data. It is recommended that a velocity measurement device capable of capturing the details of the velocity fields be employed in a future study so that the accuracy and validity of numerical results can be examined more thoroughly.

Relative Magnitude of Shear and Pressure Forces on Rigid Body

Finally, to determine the validity of the assumption that the shear forces on the rigid body surfaces are negligible, the ratio between the shear stress and the corresponding normal stress on the top, front, and bottom surfaces of the rigid body are computed from the RANS model for the three test cases at several time intervals. As a typical example, for Case III (Test L10H18P3) at $t=0.4$ s, we found that the shear to normal force ratios on the top, front, and bottom surfaces of the moving rigid body are ($0.057N$/$26.578N$) 0.21%, ($0.554N$/$78.567N$) 0.71%, and ($0.393N$/$155.960N$) 0.25%, respectively. We noted that in general, the ratio of shear to normal force at each face is less than 1% throughout the simulation period, thus validating the assumption. Because there is no experimental measurement of pressure and forces available to determine the accuracy of the numerical predictions, it is not fruitful to compare RANS and SPH numerical pressure and shear force predictions against each other.

Concluding Remarks

Two 2D numerical models—the RANS with a VOF free-surface capturing method and the SPH—have been presented. The capability and accuracy of these models are validated by comparing numerical results with experimental data involving wave generation by dropping a rigid body at various heights into a 2D flume partially filled with water (Scott Russell wave generator). In general, the numerical results from both models are in good agreement with experimental data in terms of the displacement time history of the falling cylinder and the free surface elevation time series. The RANS model appears to be able to better predict the amplitude and phase of the trailing waves than the SPH model. The SPH model consistently predicts higher dissipation of these waves at given fixed locations.

The differences in the velocity field between the two models are significant. This could be the result of different numerical resolution employed in these models. We recommend that more detailed experimental measurements of the velocity field be collected in a future study to further validate the numerical models.

Acknowledgments

Partial support from the National Science Foundation Grant Nos. CMS-9908392 and CMS-0217744, and the U.S. Office of Naval Research Grant Nos. N00014-04-10008 and N00014-06-10326 are gratefully acknowledged. Experiments and the SPH numerical simulations were funded by The Italian National Dam Office and by MIUR projects (COFIN 2004 "Onde di maremoto generate da frane in corpi idrici: meccanica della generazione e della propagazione, sviluppo di modelli previsionali e di sistemi di allerta in tempo reale basati su misure mareografiche") whose scientific coordinator is Professor Paolo De Girolamo, L'Aquila University. He is gratefully acknowledged. Finally, the writers thank the Consorzio Ricerca Gran Sasso that has provided the computer resources needed to run SPH simulations.

References

Belytschko, T., Liu, W. K., and Moran, B. (2000). *Nonlinear finite element for continua and structures*, Wiley, West Sussex, U.K.

Chang, K-A., Hsu, T.-J., and Liu, P. L.-F. (2001). "Vortex generation and evolution in water waves propagating over a submerged rectangular obstacle. Part I. solitary waves." *Coastal Eng.*, 44, 13–36.

Chang, K. A., Hsu, T.-J., and Liu, P. L.-F. (2005). "Vortex generation and evolution in water waves propagating over a submerged rectangular obstacle. Part II: Cnoidal waves." *Coastal Eng.*, 52(3), 257–283.

Chorin, A. J. (1968). "Numerical solution of the Navier-Stokes equations." *Math. Comput.*, 22, 745–762.

Di Risio, M. (2005). "Landslide generated impulsive waves: Generation, propagation and interaction with plane slopes." Ph.D. thesis, Univ. Degli Studi di Roma Tre, Rome.

Gingold, R. A., and Monaghan, J. J. (1977). "Smoothed particle hydrodynamics: Theory and application to non-spherical stars." *Mon. Not. R. Astron. Soc.*, 181, 375–389.

Hirt, C. W., and Nichols, B. D. (1981). "Volume of fluid (VOF) method for the dynamics of free boundaries." *J. Comput. Phys.*, 39, 201–225.

Hsu, T.-J., Sakakiyama, T., and Liu, P. L.-F. (2002). "A numerical model for waves and turbulence flow in front of a composite breakwater." *Coastal Eng.*, 46, 25–50.

Johnson, G. R., Stryk, R. A., and Beissel, S. R. (1996). "SPH for high velocity impact computations." *Comput. Methods Appl. Mech. Eng.*, 139, 344–373.

Lin, P. (1998). "Numerical modeling of breaking waves." Ph.D. thesis, Cornell Univ., Ithaca, N.Y.

Lin, P., and Liu, P. L.-F. (1998a). "A numerical study of breaking waves in the surf zone." *J. Fluid Mech.*, 359, 239–264.

Lin, P., and Liu, P. L.-F. (1998b). "Turbulence transport, vorticity dynamics, and solute mixing under plunging breaking waves in surf zone." *J. Geophys. Res.*, 103, 15677–15694.

Liu, P. L.-F., and Al-Banaa, K. (2004). "Solitary wave runup and force on a vertical barrier." *J. Fluid Mech.*, 505, 225–233.

Liu, P. L.-F., Lin, P., Chang, K.-A., and Sakakiyama, T. (1999). "Numerical modeling of wave interaction with porous structures." *J. Waterway, Port, Coastal, Ocean Eng.*, 125(6), 322–330.

Lucy, L. B. (1977). "Numerical approach to testing the fission hypothesis." *Astron. J.*, 82, 1013–1024.

Monaghan, J. (1994). "Simulating free surface flows with SPH." *J. Comput. Phys.*, 110, 399–406.

Monaghan, J., and Kos, A. (2000). "Scott Russell's wave generator." *Phys. Fluids*, 12, 622–630.

Monaghan, J., Kos, A., and Issa, N. (2003). "Fluid motion generated by impact." *J. Waterway, Port, Coastal, Ocean Eng.*, 129(6), 250–259.

Morris, J. (1996). "Analysis of smoothed particle hydrodynamics with applications." Ph.D. thesis, Monash Univ., Melbourne, Australia.

Panizzo, A. (2004a). "Physical and numerical modeling of subaerial landslide generated waves." Ph.D. thesis, Univ. degli studi di L'Aquila, L'Aquila, Italy.

Panizzo, A. (2004b). "SPH modelling of water waves generated by landslides." *Proc., Convegno di Idraulica e Costruzioni Idrauliche IDRA 2004*, Trento, Italy.

Panizzo, A., and Dalrymple, R. A. (2004). "SPH modelling of underwater

landslide generated waves." *Proc. ICCE 2004*, Lisbon, Portugal.
Rodi, W. (1980). *Turbulence models and their application in hydraulics—A state-of-the-art review*, IAHR.
Schlatter, B. (1999). "A pedagogical tool using smoothed particle hydrodynamics to model fluid flow past a system of cylinders." Ph.D. thesis, Dual MS Project, Oregon State Univ., Corvallis, Ore.
Shih, T. H., Zhu, J., and Lumley, J. L. (1996). "Calculation of wall-bounded complex flows and free shear flows." *Int. J. Numer. Methods Fluids*, 23, 1133–1144.
Yuk, D., Yim, S. C., and Liu, P. L. F. (2006). "Numerical modeling of submarine mass-movement generated waves using RANS model." *Comput. Geosci.*, 32, 927–935.